Femtosecond pulse compression in pressure-gas cells filled with argon

Stéphanie Champeaux and Luc Bergé
Département de Physique Théorique et Appliquée, CEA/DAM Ile de France, Boîte Postale 12, F-91680 Bruyères-le-Châtel, France
(Received 20 May 2003; published 11 December 2003)

The nonlinear propagation of femtosecond pulses in pressure-gas cells filled with argon is investigated. By increasing the pressure for reaching peak power levels close to the threshold for self-focusing, it is shown that either group-velocity dispersion or multiphoton ionizing (MPI) sources can become key players for arresting the beam collapse. For input powers noticeably above critical, MPI rapidly dominates and the formation of self-guided filaments of light occurs. We discuss the dynamical role of MPI in shortening the pulse duration up to the optical cycle limit. Two different wavelength domains are commented. The influence of space-time focusing and self-steepening effects is furthermore discussed. Their respective roles in promoting shock structures are studied and shown to still promote pulse shortening in suitable power regimes. Finally, spectral broadening is analyzed and proven to be more important for large laser wavelengths. Numerical integration of the propagation equations is explained in the light of analytical arguments.

DOI: 10.1103/PhysRevE.68.066603 PACS number(s): 42.65.Tg, 42.68.Ay, 42.65.Jx

I. INTRODUCTION

Nowadays, current techniques for spectral broadening and ultrabroadband dispersion control allow compression of intense femtosecond (fs) pulses to durations of few optical cycles. Under optimum conditions, 20-fs input pulses at infrared wavelength can be shortened down to 5 fs with an output energy up to 70 μJ [1] in pressure-gas cells or hollow-core fibers filled with noble gas at appropriate pressures. This technique yields an efficient spectral broadening caused by the interplay between self-phase modulation (SPM) and group-velocity dispersion (GVD). Postcompression of the output pulse then results in a noticeable reduction of the laser-pulse duration. Alternative techniques can also employ solid bulk materials, as glass samples [2].

So far, pulse compression has been achieved for laser peak intensity well below the threshold for multiphoton ionization (MPI), in order to just rely on low-order nonlinearities (e.g., SPM) promoting the desired spectral broadening. However, there now exists a challenging outlook as modern optical sources accessing TW powers could enable us to produce energetic pulses above the millijoule level, while keeping a short enough duration. Higher-order nonlinearities, such as plasma generation, are currently promoted by TW beams and we can wonder whether they destroy or actively contribute to the reduction of the pulse duration along the optical path. Indeed, photoinduced ionization is known not only for arresting the collapse [3] and for stabilizing the beam over long distances [4–7], but also for compressing and splitting the temporal shape of the pulse [8–10]. So, plasma formation may help in shortening laser pulses in transparent media under suitable conditions, i.e., at least as soon as the beam power exceeds the critical power for collapse, P_{cr}, for letting the beam reach ionization intensity thresholds.

The feasibility of pulse shortening strongly depends on the physical processes governing the propagation of ultrashort wave packets. Concerning the physics underlying this propagation, three principal scenarios have emerged, which we recall here briefly.

(i) *The self-waveguiding model* [4], in which self-focusing and plasma defocusing mutually balance within a static equilibrium, to produce a self-guided filament of light.

(ii) *The moving focus model* [5], where the pulse is stacked into transverse slices in the time direction. Beam collapse occurs along an extended region of the propagation axis constituted by self-focus points whose location in the longitudinal direction varies with the power engaged in the pulse slices [5,11]. The nonlinear focal region is then spread out along the propagation axis. This model pretty well describes the initial stage of optical self-focusing, but it ignores the self-guiding of light sustained by plasma defocusing beyond the beam focus [12].

(iii) *The dynamical spatial replenishment* (DSR) *model* [3], in which light guides are highly sensitive to the electron plasma created by ionization. During the focusing stage, the beam generates a narrow plasma that strongly defocuses the trailing part of the pulse and produces one leading peak in its temporal profile. Once the intensity decreases enough, plasma generation turns off. The back of the pulse can then refocus, which finally creates a two-spiked temporal profile. This event can repeat many times through focusing and defocusing cycles, so that the balance between optical self-focusing and plasma defocusing does not produce a stable static filament, but yields several dynamical equilibrium points that maintain the beam as an apparent robust structure along the propagation axis. This scenario was numerically observed for peak powers above $5P_{\mathrm{cr}}$ and later confirmed at higher power levels [13].

In connection with these scenarios, recent studies have emphasized some remarkable properties, which are worth being reminded. For instance, when only diffraction, Kerr effect, and MPI are taken into account, a femtosecond pulse with input power P_{in} very close to critical in air ($P_{\mathrm{in}} = 1.25P_{\mathrm{cr}}$) couples with the plasma generated by MPI and may evolve to a long-lived structure termed as ''gas-induced soliton'' (GIS). This behaves just as a spatial soliton in the diffraction plane and exhibits a temporal profile shrunk to a single leading peak that keeps up over considerable distances [9]. Arguments inspired from the moving-focus model were

employed to justify the existence of GIS, which revealed the possibility of reducing continuously the pulse duration by means of the defocusing action of an electron plasma. Alternatively, Nurhuda and co-workers [14], by studying the dynamics of fs pulses in argon (Ar) at input powers $P_{\rm in}=(2-3)P_{\rm cr}$, proposed that the propagation may consist in a combination of the self-waveguiding, moving-focus, and DSR models, according to the distance of the beam from the focal point. The temporal dynamics indeed seemed to follow a scenario closer to the first two scenarios near the focal point, whereas at larger distances only one narrow structure survived, which was interpreted in terms of a quasistatic balance.

In light of these possibilities, several questions regarding the basic mechanisms in ultrafast propagation remain unanswered. For instance, the ''change'' in the scenarios mentioned in Ref. [14] can be understood from the power decrease caused by multiphoton absorption (MPA), which acts in the sense of damping the temporal pulse profile into a reduced number of peaks. This suggests that the propagation dynamics is intrinsically tied to the effective ratio between the pulse power and the critical one for collapse. Therefore, the aforementioned scenarios may be unified in a unique process depending upon the defocusing properties of the electron plasma at given powers. A detailed analysis of the MPI responses according to the ratio $P_{\rm in}/P_{\rm cr}$ is thus most warranted. In addition, the role played by GVD in limiting the collapse, compared to that of MPI, is still not totally clarified. Indeed, both effects promote pulse compression and splitting along the temporal axis [11,15–18]. However, determining the power ratios at which one of the both processes may achieve the best compression remains an open problem.

Finally, at input powers close to critical, it has been shown that solitary pulses similar to the above-recalled GIS can disappear in bulk media [19,10], to the benefit of shock structures created by self-steepening and space-time focusing. Although this shock dynamics inhibits the self-guiding process to some extent, intense solitary pulses with duration compressed down to few femtoseconds can still propagate over distances close to the Rayleigh length [10]. Knowing this, it is thus worth wondering whether or not this process is generic in other media, as noble gases, for which the pressure constitutes a key parameter allowing a better control of the self-focusing threshold. In what follows, we shall therefore also discuss the incidence of pulse steepening effects on pulse compression.

The principal outlook of this paper is to provide a rather exhaustive review of the main physical processes driving the propagation of fs pulses and to emphasize the various possibilities of shortening more the pulse duration. In addition to the GVD, plasma responses and influence of pulse steepening, we moreover discuss changes in the propagation dynamics for different laser wavelengths. The interaction medium is a pressure-gas cell of argon, suitably selected to permit an easy control of the pulse power and subsequent plasma coupling for compressing the pulse duration. Basically, it is shown that the fundamental scenario governing the propagation is supplied by the DSR model, which justifies long-range propagation driven by unsteady peaks in the temporal profile. Unlike high-power beams ($P_{\rm in}/P_{\rm cr}>5$), which favor multiple temporal components distributed along the entire duration of the input pulse [20], lower-power pulses generically give rise to compressed temporal patterns alternating between two spikes that each develop with a duration close to the optical cycle over the Rayleigh length. Picking up temporal components reaching few-cycle durations in this latter range of powers thus appears to be quite promising.

The paper is organized as follows. In Sec. II, we recall the model equations governing femtosecond pulse propagation and discuss their validity in view of optimizing pulse compression and related spectral broadening. In Sec. III, the respective influences of GVD, MPI, and MPA are discussed separately for 40-fs pulses propagating in Ar cells at different pressures, ensuring tunable peak powers. It is shown that different power regimes exist, for which either GVD dominates over MPI and splits the pulse into two symmetric portions or MPI alone takes over GVD and makes the leading pulse decay into a trailing portion. In that case, introducing MPA accelerates the formation of the trail. Optical spikes with short duration can be generated over experimentally accessible distances. This study concerns lasers operating at the wavelength of 586 nm for powers close to critical. Comparison with higher-power beams inducing a longer-range propagation is also discussed. While a DSR-like dynamics fast takes place near the focus within a first focusing/defocusing cycle, a second sequence is found to promote shorter peaks at lower powers. Section IV is more devoted to changes in the pulse dynamics following variations in the laser wavelength. By investigating the UV domain (248 nm), it is found that the propagation patterns between UV and visible pulses are basically identical, up to differences in their focal points linked to their respective Rayleigh lengths. In Sec. V, pulse steepening effects are discussed. These participate through shock structures which shorten the propagation range and contribute to shrink the pulse duration. Finally, Sec. VI is devoted to spectral broadening in both UV and visible wavelength domains, with and without pulse steepening terms. At UV wavelengths, beams undergo a weak spectral broadening, unlike visible (586 nm) pulses that promote white-light generation. Throughout the different sections of this investigation, analytical arguments will be provided, in order to support the most significant aspects revealed by the numerical computations.

II. MODEL FOR PULSE PROPAGATION IN GAS

A. The propagation equations

The theoretical model for pulse propagation in gaseous media [21,19] is based on an extended nonlinear Schrödinger (NLS) equation governing the slowly varying envelope of the light electric field, coupled with an evolution equation for the electron density generated by ionization [22]. The complex scalar envelope $\mathcal{E}(r,t,z)$ of the electric field and the electron density ρ of the excited plasma evolve as

$$i\partial_z\mathcal{E}+\frac{1}{2k}T^{-1}(\Delta_\perp\mathcal{E})-\frac{k''}{2}\partial_t^2\mathcal{E}+k_0n_2T(|\mathcal{E}|^2\mathcal{E})$$
$$-\frac{k_0}{2n_b\rho_c}T^{-1}(\rho\mathcal{E})+i\frac{\beta^{(K)}}{2}|\mathcal{E}|^{2K-2}\mathcal{E}=0, \quad (1)$$

$$\partial_t\rho=\frac{\beta^{(K)}}{K\hbar\omega_0}(1-\rho/\rho_{at})|\mathcal{E}|^{2K}, \quad \rho\ll\rho_{at}, \quad (2)$$

where z is the propagation distance and t is the retarded time $(t-z/v_g)$ with v_g being the group velocity of the pulse. The transverse Laplacian describes the diffraction of axis-symmetric beams and $k''=\partial^2k/\partial\omega^2|_{\omega_0}$ is the GVD coefficient. The remaining terms in Eq. (1) account for nonlinear self-focusing related to the Kerr response of the material, defocusing due to electron plasma generation and MPA, respectively. The laser field is characterized by the linear carrier frequency ω_0 and central wave number $k(\omega_0)=n_bk_0=n_b\omega_0/c$ with the background density n_b; n_2 is the nonlinear refraction index of the gas and $\rho_c=\omega_0^2m_e\epsilon_0/q_e^2$ denotes the critical plasma density beyond which the laser pulse no longer propagates (q_e and m_e are the electron charge and mass; ϵ_0 is the electric permittivity in vacuum). $\beta^{(K)}=K\hbar\omega_0\rho_{at}\sigma_K$ is the nonlinear coefficient for K-photon absorption with MPI coefficient σ_K, where K corresponds to the minimum number of photons with energy $\hbar\omega_0$ required for liberating an electron from a medium with ionization energy U_i $[K=\mathrm{mod}(U_i/\hbar\omega_0)+1]$ and density of neutral atoms ρ_{at} at the pressure p (atm). The extended NLS equation (1) contains the principal ingredients for describing the propagation of subpicosecond optical pulses with moderate peak intensities up to 10^{14}–10^{15} W/cm^2 and powers above the GW. Optical pulse channeling results here from the competition between the transverse diffraction of the beam, normal GVD $(k''>0)$, self-focusing due to the nonlinear change in the gas refractive index, defocusing induced by MPI and related MPA. Self-steepening effects are modeled by the operator $T\equiv1+(i/\omega_0)\partial_t$ in front of the cubic nonlinearity, and space-time focusing is taken into account with T^{-1} in front of the transverse Laplacian. These operators describe the deviations from the slowly varying envelope approximation, which extends the validity of the model Eqs. (1) and (2) for pulse temporal widths decreased to the optical-cycle limit $(\tau_{o.c.}=\lambda_0/c)$ [19,23].

Several variants of the model equations (1) and (2) have been proposed in the past [3,13,14,21,22,19]. Concerning Eq. (1), we follow the derivation performed by Brabec and Krausz [23] for dealing with pulse durations up to few optical cycles. We treated the wave equation for the high-frequency electric field $\vec{E}$ by distinguishing between the second-time derivative of the polarization vector associated with the optical susceptibility of the medium and the first-order derivative in time of the current density, $\vec{J}$, attached to free-charged particle generation. The latter quantity is linked to the high-frequency electron velocity $\vec{v}_e$ and expresses at leading order as $\partial_t\vec{J}\simeq\rho q_e\partial_t\vec{v}_e$, which we reformulate by means of the electron momentum equation $\partial_t\vec{v}_e=(q_e/m_e)\vec{E}+\vec{v}_e/\tau$, involving the electron-neutral collision time $\tau\simeq10$ fs. After introducing standard envelope substitutions and eliminating the high-frequency oscillations of the carrier wave, straightforward calculations then yield $\partial_t\vec{J}\sim-i(q_e^2\rho/m_e)\omega_0\tau T(1+i\omega_0\tau T)\vec{\mathcal{E}}/[1+(\omega_0\tau)^2T^2]$. Considering here the noncollisional limit $(\omega_0\tau\gg1)$ provides a trivial dependence of $\partial_t\vec{J}$ upon the operator T, which justifies, after reversing T in the modified propagation operator $iT\partial_z\mathcal{E}$ (see Ref. [23]), the presence of the operator T^{-1} in front of the plasma coupling term of Eq. (1). This formulation slightly differs from that of Ref. [19]. The difference is, however, of secondary importance as argued below.

As far as Eq. (2) is concerned, both MPI and tunneling ionization rates should in principle contribute to ionize the medium [24,25]. Nevertheless, for ultrashort pulses with peak intensities less than 2×10^{14} W/cm^2, MPI can be expected to dominate when only singly charged ions are produced and electron-density levels are much lower than the atomic density ρ_{at}. Also, because we consider temporal compression processes from input pulses with few tens of femtoseconds only, cascade (avalanche) ionization and radiative electron recombination do not play a major role [13]. For pulse durations smaller than 50 fs, we thus ignore avalanche ionization and related plasma absorption by electron-atom collisions. MPI alone then mainly determines the mean level of free electrons, which justifies Eq. (2). As in Refs. [22,26], MPA is self-consistently introduced into Eq. (1) by, e.g., using the Poynting theorem for computing the energy balance between the MPI electron density and the related optical absorption of K photons with energy $\hbar\omega_0$ through a constant cross section.

To investigate the temporal compression of femtosecond pulses in argon, we will adopt the following physical parameters, inspired from current postcompression experiments [1] and propagation simulations [21]. We consider Gaussian input fields with a transverse waist $w_0=130\,\mu$m and a full width at half-maximum (FWHM) of irradiance $\sqrt{2\ln2}t_p=40$ fs ($t_p\simeq34$ fs) entering the beam profile

$$\mathcal{E}(r_\perp,t,0)=\sqrt{2P_{in}/\pi w_0^2}e^{-r^2/w_0^2-t^2/t_p^2}, \quad (3)$$

where $P_{\mathrm{in}}=\sqrt{2/\pi}E_{\mathrm{in}}/t_p$ denotes the input power. The optical beam is viewed as collimated at the entrance window of the pressure-gas cell. This cell is filled in with argon at pressure p and the density of neutral atoms is taken as $\rho_{at}=2.7\times10^{19}p$ cm^{-3}. Beams are centered on two possible different laser wavelengths, namely, $\lambda_0=586$ nm or $\lambda_0=248$ nm, with associated Rayleigh lengths $z_0\equiv\pi n_bw_0^2/\lambda_0\simeq9.1$ cm and $z_0\simeq21.4$ cm, respectively. GVD coefficients then take the respective values $k''=0.26p$ fs^2/cm and $k''=1.21p$ fs^2/cm. The medium is characterized by the Kerr refraction index $\tilde{n}=n_b+n_2|\mathcal{E}|^2$ with $n_b=1+2.7\times10^{-4}p$, $n_2=4.9\times10^{-19}p$ cm^2/W at 586 nm [21] and $n_2=2.9\times10^{-19}p$ cm^2/W at 248 nm [7]. So, the critical power for self-focusing, defined by $P_{\mathrm{cr}}=\lambda_0^2/2\pi n_bn_2$, decreases as the pressure is increased $(n_2\sim p)$. At constant energy $E_{\mathrm{in}}=40\,\mu$J, the ratio $P_{\mathrm{in}}/P_{\mathrm{cr}}$ is thus augmented in turn. Follow-

ing Ref. [21] and Keldysh pioneering paper [24], pulses ionize Ar atoms with gap potential $U_i=15.76$ eV from MPI processes characterized by the coefficient $\sigma_K=5.36\times10^{-99}\ \mathrm{s}^{-1}\,\mathrm{cm}^{2K}/\mathrm{W}^K$, which yields the number of photons $K=8$ at wavelength $\lambda_0=586$ nm. In the UV domain ($\lambda_0=248$ nm), recent experimental measurements [27] emphasized pressure-independent MPI coefficients σ_K for various atmospheric gaseous species. These coefficients were mostly found consistent with anterior predictions obtained by the nonresonant Keldysh theory. However, concerning argon, wide discrepancies between the experimentally measured ionization coefficients and the Keldysh numbers were reported, i.e., the ionization coefficients were measured to rank between 3.7×10^{-41} and $1.4\times10^{-44}\,\mathrm{s}^{-1}\,\mathrm{cm}^{2K}/\mathrm{W}^K$ at two different pressures, far above the Keldysh's rate $4.6\times10^{-47}\,\mathrm{s}^{-1}\,\mathrm{cm}^{2K}/\mathrm{W}^K$ [27]. The possibility of exciting partial resonances was invoked for explaining these discrepancies. Knowing this, we shall thus opt for an intermediate value of σ_K at 248 nm, i.e., $\sigma_K=1.5\times10^{-44}\,\mathrm{s}^{-1}\,\mathrm{cm}^{2K}/\mathrm{W}^K$, involving the number of photons $K=4$ at $\lambda_0=248$ nm. Note that this choice is viewed as a natural compromise among the MPI cross sections available in the literature. It guarantees that the maximum intensity required for reaching a balance between self-focusing and ionization ($I_{\max}\propto\sigma_K^{1/1-K}$) will not differ by more than one decade from those attainable with the other two extreme (Keldysh or experimental) cross sections. This selected MPI rate is furthermore compatible with an ionization mainly driven by multiphoton processes, since the Keldysh parameter $\gamma=(\omega_0/q_e|\mathcal{E}|)\sqrt{2m_eU_i}$ remains above the unity with maximum laser intensities $I_{\max}\equiv|\mathcal{E}|^2_{\max}<10^{15}$ W/cm^2.

From the numerical point of view, Eq. (1) is solved in axially symmetric geometry by means of a Fourier spectral decomposition in time and a standard Cranck-Nicholson in space, applied to each spectral component. Equation (2) is solved by a semianalytical integration and is directly integrated as a function of the numerically-computed intensity from the initial density value $\rho(t\to-\infty)=10^9\ \mathrm{cm}^{-3}$ (for more details, see Ref. [20]). Calculations were performed within a numerical box of either 621×2048 or 2001×2048 points in the (r,t) dimensions. High resolution was achieved by means of the integration steps $\Delta r/w_0=1-5\times10^{-3}$, $\Delta t/t_p=2-3\times10^{-3}$, whereas the increment in z was currently $\Delta z/4z_0<10^{-4}$.

B. The dimensionless equations

In order to argue on the relevant mechanisms participating in the temporal shortening of fs pulses in Ar, we find it convenient to rescale Eqs. (1) and (2) in a dimensionless form. We introduce the substitutions $r\to w_0r$, $t\to t_pt$, $z\to4z_0z$, $\mathcal{E}\to\sqrt{P_{\mathrm{cr}}/4\pi w_0^2}\psi$ and $\rho\to(n_b\rho_c/2z_0k_0)\rho$, and reexpress the model equations as follows:

$$i\partial_z\psi+\nabla_\perp^2\psi+(|\psi|^2-\rho)\psi+\mathcal{F}(\psi)=0, \tag{4}$$

$$\partial_t\rho\simeq\Gamma|\psi|^{2K}, \tag{5}$$

$$\mathcal{F}\simeq-\delta\partial_t^2\psi+i\nu|\psi|^{2K-2}\psi+\frac{i}{t_p\omega_0}\partial_t(|\psi|^2\psi-\nabla_\perp^2\psi+\rho\psi). \tag{6}$$

In Eq. (6), $\mathcal{F}(\psi)$ includes leading-order perturbations (GVD, MPA, pulse steepening terms). It follows from a direct Taylor expansion of the operator T^{-1} for an envelope frequency assumed to be smaller than ω_0. The function $\mathcal{F}$ involves GVD and MPA with normalized coefficients $\delta\equiv2z_0k''/t_p^2$ and $\nu=2z_0\beta^{(K)}(P_{\mathrm{cr}}/4\pi w_0^2)^{K-1}$, respectively. The rescaled MPI coefficient reads $\Gamma=(2z_0k_0/n_b\rho_c)\sigma_K\rho_{\mathrm{at}}t_p(P_{\mathrm{cr}}/4\pi w_0^2)^K$. Note that δ, ν, and Γ vary with the gas pressure p as $\beta^{(K)}\sim p$, $P_{\mathrm{cr}}\sim1/n_2\sim1/p$ and $\rho_{\mathrm{at}}\sim p$.

In the coming sections, the behavior of the rescaled wave field ψ will be commented for gas pressures ensuring an effective power ratio $P_{\mathrm{in}}/P_{\mathrm{cr}}$ above the unity. In that case, it is known that the wave field first develops a critical collapse and tends to the self-similarly compressing shape

$$\psi(r,z,t)\to\frac{\sqrt{I(z,t)}}{R(z,t)}\phi(\xi)e^{iS(z,t)}, \tag{7}$$

with $S(z,t)=\zeta(z,t)+R_z(z,t)R(z,t)\xi^2/4$, where $\zeta(z,t)\equiv\int_0^z du/R^2(u,t)$ and $I(z,t)$ represents an amplitude factor satisfying $I_z=0$ when the beam collapses in a conservative way. Here, we have introduced the new spatial variable $\xi\equiv r/R(z,t)$, rescaled with respect to the (z,t)-varying radius $R(z,t)$ of the beam envelope. As collapse takes place at a finite propagation distance $z_c(t)$ fixed by the temporal distribution of the input pulse, the radius $R(z,t)\sim[z_c(t)-z]^{1/2}$ vanishes, which implies the divergence of the beam amplitude. The radial shape of ψ then relaxes to the so-called Townes mode ϕ, which is the unique radially symmetric positive solution of the solitary-wave equation $-\phi+\nabla_\perp^2\phi+\phi^3=0$ with power $P_c\equiv\int\phi^2dxdy=11.68$. Conservation of the transverse power $P\equiv\int|\psi|^2d\vec{r}$ when $\mathcal{F}=0$ then requires $I(t,z)=\alpha P_{\mathrm{in}}e^{-2t^2}/P_{\mathrm{cr}}$ where $\alpha=4\pi/11.68$ [28–30].

To discuss the action of the different perturbations entering $\mathcal{F}$, we shall develop a variational approach expounded in Ref. [31]. This method provides results comparable with the ''modulation method'' previously derived in Ref. [30], when we consider the limits $R(z,t)\to0$ and $|R_zR|\ll1$, which characterize a critical collapse. It consists in plugging Eq. (7) into the dynamical relations governing the mean-squared radius of the beam and the power conservation law. Under the former limits, direct application of this variational principle to Eqs. (4)–(6) yields the reduced dynamical equations

$$\frac{M}{4P_c}R^3R_{zz}\simeq1-I-\frac{R^2}{2P_c}\int\phi^2\xi\partial_\xi\rho d\vec{\xi}, \tag{8}$$

$$\frac{I_z}{I}\simeq2\delta\zeta_{tt}-2\nu A\frac{I^{K-1}}{R^{2K-2}}-\frac{1}{t_p\omega_0}\left[B(R^{-2})_t+2\Gamma C\frac{I^K}{R^{2K}}\right], \tag{9}$$

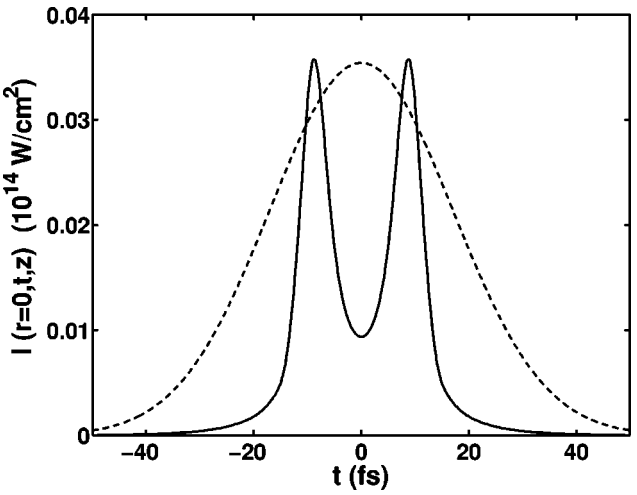

FIG. 1. Temporal profiles of a 40-fs Gaussian pulse in Ar at the pressure $p=1.2$ atm ($P_{\rm in}/P_{\rm cr}=1.011$) for the wavelength $\lambda_0=586$ nm. (a) $z=0$ cm, (b) $z=45.6$ cm.

where $M=\int \xi^2\phi^2 d\vec{\xi}$, $A=\int \phi^{2K} d\vec{\xi}/P_c$, $B=3I+1$, and $C=\int \phi^{2K+2} d\vec{\xi}/P_c$. Equation (9) originates from the power variations $\partial_z P=-2\,\mathrm{Im}\int[\psi^*\mathcal{F}(\psi)]d\vec{r}$, whose right-hand side (RHS) is treated perturbatively ($\mathcal{F}\ll 1, I_z/I\ll 1$). Here, the first term refers to GVD, the second one to MPA and the last term models pulse steepening deviations. Among those, we can omit the last contribution of Eq. (9) coming from the variations in time in front of the coupling term ($\rho\mathcal{E}$) in Eq. (1). This correction, compared with the MPA contribution of Eq. (9), is relevant whenever $I/R^2 \geqslant (t_p\omega_0)\nu A/\Gamma C$. Straightforward estimates of this inequality imply that the beam radius should currently go down below 10% of its input value for making the last term of Eq. (8) significant. In the coming simulations, this constraint is never fulfilled and, therefore, temporal variations from the original time derivative $T^{-1}(\rho\mathcal{E})$ can henceforth be omitted.

III. SELF-FOCUSING VERSUS GVD, MPI, MPA AT VISIBLE WAVELENGTH

A. Self-focusing versus group velocity dispersion

To start with, we investigate the roles of GVD, MPI, and MPA at the visible wavelength $\lambda_0=586$ nm, as the gas pressure is increased to supply power ratios higher than critical. In this scope, let us first discuss the influence of GVD for $P_{\rm in}/P_{\rm cr}$ very close to unity. Fixing $p=1.2$ atm, the power ratio is equal to 1.011. The numerical solving for Eqs. (1) and (2) then shows that the arrest of collapse is not promoted by MPI, whose electron density never exceeds 10^{12} cm^{-3} and the peak intensity remains limited to $I_{\max}<1.5\times 10^{13}$ W/cm^2. Instead, GVD is the main process stopping the collapse, by splitting the pulse into two symmetric [leading ($t<0$) and trailing ($t>0$)] subpulses. Thus, even in focusing regimes, provided Ar pressure is low enough, the pulse undergoes a symmetric splitting, which arrests the self-focusing and thereby plasma formation. Figure 1 displays the temporal profiles of the pulse intensity at the beam center ($r=0$) for the propagation distances $z=0$ cm (dashed line) and $z=45.6$ cm (solid line), once GVD splitting has saturated the collapse. GVD induces a temporal compression [11], which already reduces the overall (FWHM) duration of the pulse by a factor ~ 2.

This observation is compatible with earlier works in the field, following which the smaller the dispersion coefficient, the lower the splitting threshold [16,18]. Consequently, for input peak power near enough critical, GVD can dominate self-focusing for sufficiently small dispersion coefficients. Note that this property does not exclude significant dispersion effects at very high pressures, $\delta\sim p\to+\infty$, for which GVD in argon also becomes a key player in the pulse dynamics [21].

From a more analytical point of view, GVD splitting can be understood from the reduced model, Eqs. (8) and (9), by considering collapsing pulses whose each time slice self-focuses at the longitudinal distance:

$$z_c(t)\simeq Z_0\left[\alpha\frac{P_{\rm in}}{P_{\rm cr}}e^{-2t^2}-1\right]^{-\beta}, \tag{10}$$

with $Z_0\simeq 0.16$, $\beta\simeq 0.635$. Formula (10) provides reasonable estimates of nonlinear focal points as long as $P_{\rm in}/P_{\rm cr}<2$ [30]. For Gaussian pulses, the central time slice focuses at the maximum distance $z_c(t=0)$; $z_c(t)$ and $\dot{z}_c(t)$ both reach infinity as t tends to the caustics $\pm t^*$, where

$$t^*=-[\ln\sqrt{\alpha P_{\rm in}/P_{\rm cr}}]^{1/2}. \tag{11}$$

Furthermore, $\dot{z}_c(t)$ is positive for $t>0$ and negative for $t<0$ [$\dot{z}_c(0)=0$], whereas $\ddot{z}_c(t)$ always remains positive. Basically, GVD action is governed by the first term in the RHS of Eq. (9). Near the collapse distance, ansatz (7) allows us to replace all time derivatives as follows: $\partial_t=-\dot{z}_c\partial_z$, $\partial_t^2=-\ddot{z}_c\partial_z+\dot{z}_c^2\partial_z^2$ [16], which yields

$$\frac{I_z^{\rm GVD}}{I}=2\delta(-\ddot{z}_c/R^2+\dot{z}_c^2(1/R^2)_z). \tag{12}$$

In the vicinity of the most powerful time slice ($t=0$), $\dot{z}_c\simeq 0$ and Eq. (12) describes a defocusing around the central slice: The pulse power is transferred towards nonzero times, symmetrically located with respect to $t=0$. This estimate refinds the results formerly derived by Fibich and Papanicolaou [30]. Concerning the domination of GVD over MPI in the present configuration, we may employ the following arguments. Let us assume that collapse is first stopped at the time slice with maximum power, i.e., at times close to $t=0$. On the one hand, by using Eq. (7), saturation of the self-focusing by MPI signifies $|\psi|^2\sim\rho$ and, therefore,

$$I\phi^2/R_{\rm min}^2\sim\Gamma(\phi^{2K}/R_{\rm min}^{2K})\int_{-\infty}^{t}I^K(t')dt'$$
$$\sim(\Gamma/\sqrt{K})(5.2P_{\rm in}/P_{\rm cr})^K R_{\rm min}^{-2K}, \tag{13}$$

which is estimated by means of $\phi_{\max}=\phi(\xi=0)=2.2062$. $R_{\min}\sim 2\sqrt{P_{\rm in}/P_{\rm cr}}(\Gamma/\sqrt{K})^{1/2(K-1)}$ is the minimum beam radius reached at the smallest collapse distance. On the other hand, GVD contribution mainly scales as $-\delta\partial_t^2\psi/\psi \sim \ddot{z}_c(0)\delta/R^2$, where $\ddot{z}_c(0)=4\beta z_c(0)/(1-P_{\rm cr}/\alpha P_{\rm in})$. To make GVD dominate over Kerr and MPI, it is sufficient to fulfill the inequality

$$\ddot{z}_c(0)\,\delta/R^2 \gg I\phi^2/R^2, \tag{14}$$

which is equivalent to $C\delta > (\alpha P_{\rm in}/P_{\rm cr}-1)^{\beta+1}$, where C is a constant of order unity. Hence, GVD takes over both Kerr and MPI whenever

$$\alpha\frac{P_{\rm in}}{P_{\rm cr}} < 1+(C\delta)^{1/(\beta+1)}. \tag{15}$$

This inequality restores the curve of Luther *et al.* [17], separating the regions of GVD splitting from Kerr-dominated regimes in the plane $(P_{\rm in}/P_{\rm cr},\delta)$, when $C\simeq 2.6$ (see also Ref. [15]). As we can see, these regions emerge either at high pressure (large δ's) or at powers very close to critical if δ is weak. With $\delta=4.9\times10^{-3}$ for $p=1.2$ atm, the latter condition applies to the configuration illustrated in Fig. 1.

B. Multiphoton regime

From estimates (13) and (14), GVD scales as $\sim\ddot{z}_c(0)\delta/R^2$, Kerr response as $I\phi^2/R^2$, whereas MPI behaves as $(\Gamma/\sqrt{K})(5.2P_{\rm in}/P_{\rm cr})^K R^{-2K}$. So, MPI may become a key player when Eq. (15) is no longer fulfilled and when the beam waist $R(z,t)$ decreases enough, even for moderate values of $P_{\rm in}/P_{\rm cr}$. As the cell pressure is increased, the power ratio increases in turn and the self-focusing dynamics overcomes GVD to the benefit of plasma formation. Numerically, MPI-dominated regimes were observed to take place from ratios $P_{\rm in}/P_{\rm cr}$ above 1.095, which is fully compatible with Eq. (15).

The action of MPI is to deplete the pulse temporal profile through an ionization front that defocuses the trailing portion of the pulse. Because the time slices mostly self-focus in the time domain $|t|<|t^*|<1$, we can assume that the time variations in $R(z,t)$ are relatively flat compared with e^{-2Kt^2} and integrate Eq. (5) to find

$$\rho(r,t,z)\simeq\sqrt{\frac{\pi}{8K}}\,\Gamma\left(\alpha\frac{P_{\rm in}}{P_{\rm cr}}\phi^2\right)^K\frac{{\rm erf}(\sqrt{2K}t)+1}{R^{2K}[z_c(t)-z]}, \tag{16}$$

where $\rho(t\to-\infty)$ has negligible values. The last term in Eq. (8) then scales as $R^{2(1-K)}\partial_\xi\rho$ where $\partial_\xi\rho\sim\partial_\xi\phi^{2K}$ is negative. As $R\to R_{\min}$, all time slices belonging to the interval $t>0$ are defocused. However, at negative times, the pulse continues to self-focus and feeds plasma defocusing until forming a single time slice located near $t=t^*$ [9,8].

Figure 2 displays temporal profiles of the pulse intensity at $r=0$ for the laser wavelength $\lambda_0=586$ nm and for $p=1.8$ atm corresponding to the associated ratio $P_{\rm in}/P_{\rm cr}=1.517$. Panel (a) displays the temporal profile at two propagation distances when MPA effect is discarded. Panel (b) displays the changes introduced when both MPI and MPA are retained: Nonlinear dissipation damps the intensity growth earlier along the z axis and permits the emergence of a trailing peak within a pulse envelope of $\sim$30 fs FWHM duration (dotted curve). The trail then sustains the propagation at later distances.

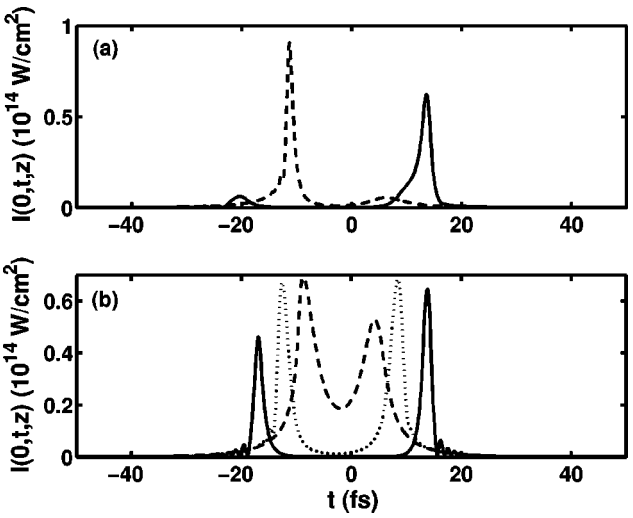

FIG. 2. Single- and double-peaked temporal profiles of 40-fs Gaussian pulse in Ar with $p=1.8$ atm ($P_{\rm in}/P_{\rm cr}=1.517$) and $\lambda_0=586$ nm at the propagation distances (a) $z=10.5$ cm (dashed curve), $z=20.5$ cm (solid curve) without MPA; (b) $z=9.24$ cm (dashed curve), $z=11.5$ cm (dotted curve), $z=15.25$ cm (solid curve) with MPA included.

In physical units, MPI counterbalances self-focusing at laser intensities $I_{\max}\sim\rho^{\max}/2\rho_c n_2=(2\rho_c n_2/\Delta t\sigma_K\rho_{\rm at})^{1/K-1}\approx 7\times10^{13}$ W/cm^2, where $\rho^{\max}\approx\Delta t\sigma_K\rho_{\rm at}I_{\max}^K\simeq 4\times10^{17}$ cm^{-3} for a time scale Δt of order t_p. Plasma formation is, as expected, accompanied by a sharp duration shortening of the front pulse reached near the instant $t^*t_p\simeq-16$ fs [Fig. 2(a), dashed curve]. At lower pressures ($p=1.55$ atm, $P_{\rm in}/P_{\rm cr}=1.3$), this leading edge slowly diffracts without giving rise to a growing trailing peak. Excitation of a trail instead occurs at higher powers. In the configuration shown in Fig. 2(a) ($p=1.8$ atm, $P_{\rm in}/P_{\rm cr}=1.517$), the leading peak is unstable: small fluctuations in the maximum intensity produce significant decreases in the ionization level ($\delta\rho/\rho_{\max}\sim K\delta I/I_{\max}$), which allows the growth of a symmetric trail containing enough power for self-focusing. Leading as well as trailing spikes can attain 2 fs duration, inside a single peaked distribution covering propagation distances up to one Rayleigh length. Thus, at low powers $<2P_{\rm cr}$, MPI can shrink the pulse duration to one optical cycle ($\lambda_0/c\simeq1.95$ fs) within a singly peaked profile.

With MPA, the leading component is partly damped in the intensity ratio $I_z/I\simeq-2\nu A(I/R^2)^{K-1}$, as the peak electron plasma forms a density plateau. Consequently, the beam power diminishes [31]; the electron density attains lower levels and permits the emergence of a trailing portion earlier than in the former case. This configuration is shown in Fig. 2(b). The back of the pulse, although decreased in amplitude, keeps an intensity close to $\sim I_{\max}$ over half of one Rayleigh

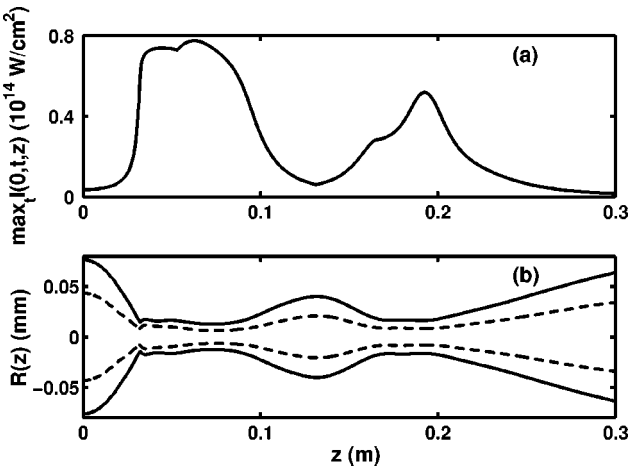

FIG. 3. Propagation ranges of 40-fs pulses in Ar with $p=3.6$ atm ($P_{in}/P_{cr}=3.035$) at $\lambda_0=586$ nm. (a) Peak intensity; (b) pulse transverse diameter [$R(z)$ is defined as the FWHM radius of the fluence distribution $\mathcal{F}=\int_{-\infty}^{+\infty}|\mathcal{E}(t)|^2dt$].

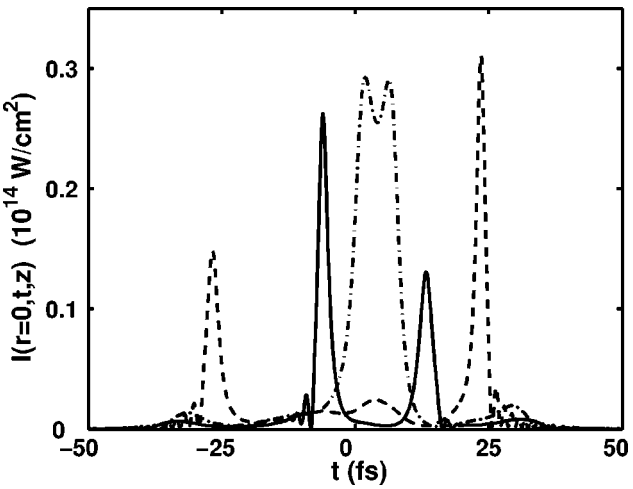

FIG. 4. Same configuration as in Fig. 3. Temporal profiles are shown along the second focusing/defocusing sequence: $z=10$ cm (dashed line), $z=17$ cm (dash-dotted line), and $z=21$ cm (solid line).

length. Even though the pulse profile has decayed into two peaks, *the trail remains dominant with duration of less than two optical cycles*. A similar property was discovered for fused silica in Ref. [10], where estimates of the MPA-damped propagation range can be found.

C. Higher-power regime

Next, we increase the pressure to $p=3.6$ atm, which leads to the effective power ratio $P_{in}/P_{cr}=3.035$. In that case, the pulse develops two focusing/defocusing sequences shown in Fig. 3(a). In the diffraction plane, the beam waist is reduced by a factor $\sim 1/5$, while the pulse attains its maximum intensity. When computing the beam diameter as the FWHM of the fluence distribution, we observe the appearance of a ''self-guided'' channel of light which covers a total distance of two Rayleigh lengths in the present configuration [Fig. 3(b)].

Visual inspection of the numerical results reveals that doubling the input power amounts to repeating over longer propagation distances the temporal dynamics displayed in Fig. 2(b). In the first focusing/defocusing cycle the pulse time profile is depleted to a front peak whose partial damping by MPA enables the excitation of a 2-fs trailing portion that dominates from $z\simeq 0.08$ m. As the trail diffracts, power is reinjected at the center ($t\rightarrow 0$) from $z\simeq 1.4$ m. A new sequence of temporal distortions then occurs. This second sequence, emphasized in Fig. 4, is supported by a ~ 9-fs narrow structure that further decomposes into a shrunk leading spike of ~ 2.5 fs duration and a small trail. With a power being less than half of P_{in} (E_{in} decreases to $E_{in}/2$ after $z=170$ mm), the central wave packet undergoes plasma defocusing as in Fig. 2, but only gives rise to a dominant narrow leading peak. This pattern may be compared with the asymptotic propagation stage shown by Nurhuda *et al.* in Ref. [14]: the beam power starting from 3 critical powers decreases after a few meters of propagation. When a second focusing sequence occurs, it acts over a narrow peak with weaker power, capable of being still compressed to very short durations. This propagation pattern first follows a fast DSR at high power, leading to a rapid splitting of the pulse as proposed by Mlejnek *et al* [21]. It ends with a smoother defocusing sequence at lower power, favoring the emergence of one dominant, very short subpulse.

By comparison with Sec. III B, the propagation scenario is found to be similar for the two ratios P_{in}/P_{cr} investigated. However, sharp distortions in the pulse occur over shorter distances at higher powers. For this reason, picking up laser-pulse components with reduced durations might be more convenient from an experimental point of view at beam powers closer to critical.

IV. INFLUENCE OF THE LASER WAVELENGTH

For a few years, differences have been expected in the filamentation regime, when changing the laser wavelength from, e.g., infrared to ultraviolet. Experimental observations of fs pulses in the atmosphere indeed reported salient differences in the intensity levels reached by the beam ($I_{max}\sim 10^{14}$ W/cm^2 for $\lambda_0=800$ nm, $I_{max}\sim 10^{12}$ W/cm^2 for $\lambda_0=248$ nm), as well as in the free electron densities accessible experimentally at different wavelengths [32,33]. Only recently [34] this controversy was resolved by solving numerically propagation equations involving two species (nitrogen/oxygen), for 50-fs input Gaussian pulses with comparable energies ($E_{in}=3$ mJ for $\lambda_0=800$ nm; $E_{in}=1$ mJ for $\lambda_0=248$ nm; the difference in energy enabled the self-guided filament to start from the same focus point). Up to differences in the number of focusing/defocusing cycles linked to the ratio P_{in}/P_{cr} (higher for UV beams as $P_{cr}\sim\lambda_0^2$), the characteristic dynamics in the propagation was revealed to be the same for the two wavelengths. In particular, macroscopic quantities, as the maximum intensity levels $I_{max}\sim 10^{13}$–10^{14} W/cm^2 and the peak electron density $\rho_{max}\sim 10^{17}$ cm^{-3} were quite comparable. The most important difference lay in the spectral broadening, much larger in the IR

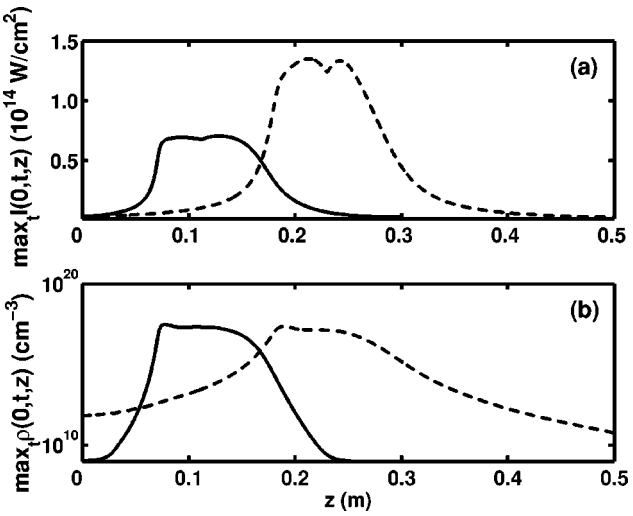

FIG. 5. Comparison of (a) peak intensities and (b) maximum electron densities from the Gaussian condition (3) for UV (248 nm, dashed curve) and visible (586 nm, solid curve) wavelengths at comparable power ratios $P_{\rm in}/P_{\rm cr}=1.531$ and $P_{\rm in}/P_{\rm cr}=1.517$, respectively.

domain than in the UV domain. The aforementioned variations were explained by means of averaging procedures in the experimental diagnostics, which may change from one setup to the other.

In the present context, we find it instructive to check the comparison between the first-chosen visible wavelength ($\lambda_0=586$ nm) and UV beams ($\lambda_0=248$ nm) under the physical parameters defined in Sec. II. Unlike in Ref. [34], we do not make the beam energies differ between the two wavelengths. Instead, we conserve the same power ratio for the two λ_0's ($P_{\rm in}/P_{\rm cr}\simeq 1.5$). Figure 5 shows the propagation ranges emphasizing the peak intensities and associated electron densities, which confirm the previous expectations. Again there is no significant difference in the macroscopic characteristics of the propagation. The peak intensities $I_{\max}$ and maximum densities $\rho_{\max}$ are of the same order of magnitude for both wavelengths. In the UV domain we indeed evaluate $I_{\max}\approx 2\times 10^{14}$ W/cm^2 and $\rho_{\max}\approx 3\times 10^{17}$ cm^{-3}, which are close to their counterparts at $\lambda_0=586$ nm.

Apart from the shift in the nonlinear focus point that only depends on the change in the Rayleigh length [$z_c(0)\propto z_0\sim\lambda_0^{-1}$], the self-guiding length appears to be identical at a level of free electrons exceeding 10^{17} cm^{-3}. The self-channeling length, defined by the damping of the maximum intensity by MPA, i.e., $\Delta z_{\rm MPA}\sim(\beta^{(K)}I_{\max}^{K-1})^{-1}$, is of the same magnitude for both wavelengths. Further inspection of the temporal profiles shows that UV pulses follow the same route as in Fig. 2(b), by decaying first into a leading peak, then into a trail. This produces a two-peaked structure, with a prominent trailing portion that sustains the self-guided channel of light. This dynamical picture is characteristic of the DSR scenario. The notch in $\max_t I$ (both solid/dashed curves) occurs when the trailing peak takes over the leading one. Visible differences, however, appear in the pulse spectra, which will be commented in Sec. VI.

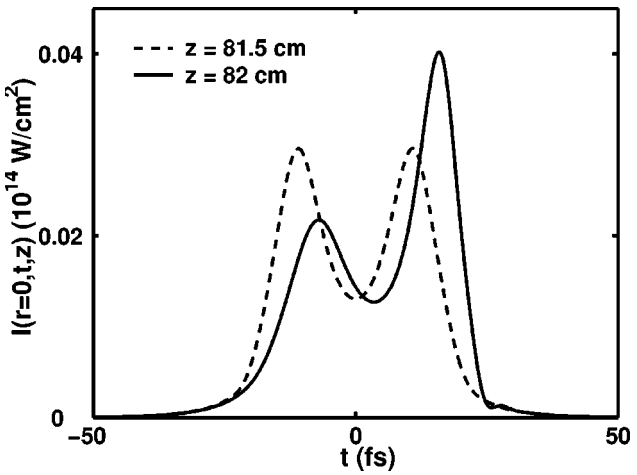

FIG. 6. Influence of the operators T, T^{-1} at a low-power regime ($p=0.38$ atm, $P_{\rm in}/P_{\rm cr}=1.058$) for $\lambda_0=248$ nm. Solid and dashed curves show temporal profiles with and without pulse steepening terms in a GVD-dominated regime.

V. SELF-STEEPENING AND SHOCK DYNAMICS

We now discuss the influence of self-steepening terms, i.e., the deviations from the slowly varying envelope approximation giving rise to space-time focusing [$T^{-1}\nabla_\perp^2\mathcal{E}$] and self-steepening [$T(|\mathcal{E}|^2\mathcal{E})$] effects in Eq. (1). To gain a deeper insight into their action in the pulse dynamics, let us employ the variational approximation derived in Sec. II. From Eq. (6), those perturbations are responsible for a loss of power governed by the relation $I_z^{\rm steep}/I\simeq-(t_p\omega_0)^{-1}B(1/R^2)_t$, where $B=3I+1$. Employing the substitution $\partial_t=-\dot{z}_c\partial_z$ near the first collapsing time slice [$R_z<0$ as $z\to z_c(t\sim 0)$], the deviation attached to pulse steepening terms induces the intensity loss

$$I_z^{\rm steep}/I\simeq(t_p\omega_0)^{-1}2B\dot{z}_c[1/R^2]_z, \tag{17}$$

with $[1/R^2]_z>0$. From this estimate we see that, whereas GVD causes a symmetric pulse splitting with respect to the center $t=0$, pulse steepening produces a transfer of power from the leading portion of the pulse ($\dot{z}_c<0$) to the trailing one ($\dot{z}_c>0$). Similar power transfers were expected in Ref. [35] and numerically observed in [36]. Applied to UV pulses in argon at powers for which plasma growth is stopped by GVD ($P_{\rm in}/P_{\rm cr}=1.058$), this dynamics creates a strong asymmetry in the pulse temporal profile, which is illustrated in Fig. 6.

At higher powers ($P_{\rm in}/P_{\rm cr}=1.5$) reached with setting $p=0.55$ atm, MPI takes over GVD in arresting the collapse. Omitting GVD and MPA for simplicity, we here consider a self-focusing regime in which nonlinearities dominate transverse diffraction. Following Anderson and Lisak [37], we may then employ the substitution $\psi=Ae^{i\varphi}$ to derive the equations for the amplitude and phase of the solution ψ:

$$\varphi_z+\frac{A^2}{t_p\omega_0}\partial_t\varphi=A^2-\rho, \tag{18}$$

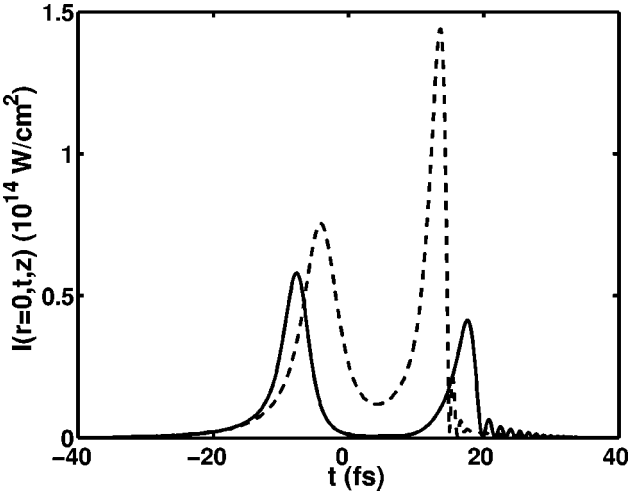

FIG. 7. Temporal distributions of a 40-fs Gaussian pulse propagating in Ar with $\lambda_0=248$ nm, $p=0.55$ atm, $P_{\rm in}/P_{\rm cr}=1.531$ at $z=21.65$ cm (dashed line), where a shock develops on the trail being shrunk to ~ 3 fs in duration, and at $z=25$ cm (solid line), where the shock disperses rapidly.

$$A_z+\frac{3}{t_p\omega_0}A^2\partial_t A=0. \tag{19}$$

Equation (19) admits the generic solution $A^2=F(t-3zA^2/t_p\omega_0)$, where F is the intensity profile of an "initial" pulse unaffected by the self-steepening term. Considering, e.g., a sech-shaped optical distribution as $A^2=A_0^2\,\mathrm{sech}(\tau)$ where $\tau\equiv(t-t_0)/\tau_0$ for a pulse located initially at the time slice $t=t_0$ with a duration τ_0, Eq. (19) links A^2 and τ through the relation

$$\tau=3Q\frac{A^2}{A_0^2}+\cosh^{-1}\left[\frac{A_0^2}{A^2}\right], \tag{20}$$

where $Q\equiv zA_0^2/t_p\omega_0\tau_0$. Within the present approximations, it is found by differentiating Eq. (20) with respect to time that a shock singularity ($A_t^2\to\infty$) develops at $z\to z_{\rm shock}=2t_p\omega_0\tau_0/3A_0^2$, when z attains the limit fixed by $Q\to 2/3$. Strong temporal gradients arise on the trailing edge of the pulse, which forms a shock structure. Such a shock is shown in Fig. 7 for UV beams with powers equal to 1.5 times critical (dashed line). At later propagation distances, the enhanced trailing portion reinjects power to the leading remanent of the pulse (solid line), which finally diffracts.

Figure 8 shows examples of steepened profiles for both $\lambda_0=586$ nm (dash-dotted line) and $\lambda_0=248$ nm (solid line) from 40-fs Gaussian pulses solved with the complete set of Eqs. (1) and (2). For comparison, we have reported in dashed line the temporal distribution emerging without pulse steepening at neighboring longitudinal distances. Although the shock dynamics enhances the trailing portion earlier in the propagation range, no singularity is formed and the intensity level in the trailing peak is limited to values remaining comparable with those of pulses that are not subject to the operators T, T^{-1}.

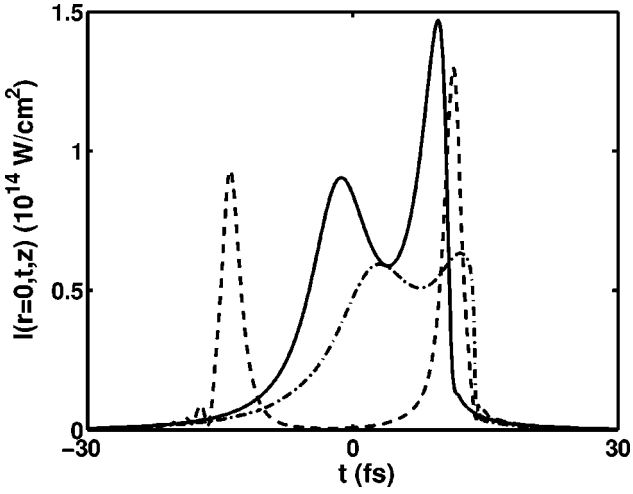

FIG. 8. Steep profiles with or without the T, T^{-1} operators. The solid curve shows temporal distribution of the 40-fs Gaussian pulse undergoing steepening effects at $z=20$ cm for $P_{\rm in}/P_{\rm cr}=1.531$ and $\lambda_0=248$ nm. The dashed curve represents the same beam in the limit T, $T^{-1}\to 1$ at $z=25$ cm. The dash-dotted curve refers to the Gaussian beam with $\lambda_0=586$ nm, undergoing strong temporal gradients caused by the operators T, T^{-1} at $z=8.25$ cm.

Figure 9 illustrates the behavior of the peak intensity with and without pulse steepening. In the presence of these effects, the shock structure shortens the length of the self-guided filament, which diffracts earlier. In spite of this, we can notice that the basic structure inspired from the DSR scenario emphasizing first the formation of a leading peak followed by that of a trail resulting in a double-peaked structure is still conserved with space-time focusing and self-steepening. The only difference is the noticeable enhancement in the amplitude undergone by the trailing portion. Pulse steepening contributes to shrink the pulse in time (see Fig. 8, where the FWHM temporal extension of the wave packet is about 15 fs) over distances still close to the Rayleigh range.

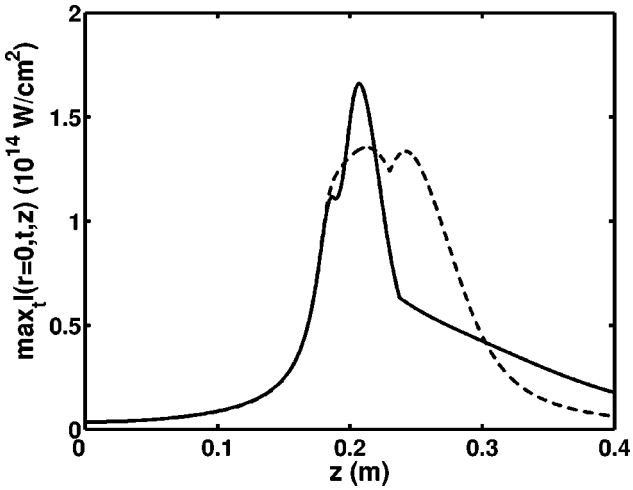

FIG. 9. Propagation range of an UV Gaussian pulse at $p=0.55$ atm, $P_{\rm in}/P_{\rm cr}=1.531$. Solid curve illustrates the role of self-steepening effects. Dashed curve results from simulations constrained to $T=T^{-1}=1$.

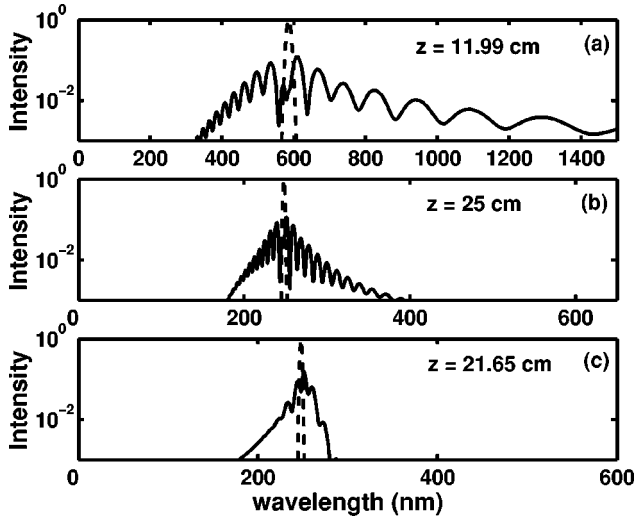

FIG. 10. Power spectra for 40-fs pulses with power $P_{\rm in}/P_{\rm cr} \simeq 1.5$ at the wavelengths: (a) $\lambda_0 = 586$ nm, (b) $\lambda_0 = 248$ nm without pulse steepening terms, and (c) $\lambda_0 = 248$ nm with pulse steepening terms. Dashed lines represent the input spectrum at $z = 0$. Intensity axis is expressed in arbitrary units.

VI. SPECTRAL BROADENING

To achieve this investigation, we here discuss spectral broadenings caused by the interplay between self-phase modulation (Kerr response), MPI, and pulse steepening. On the one hand, characterizing the ability of fs pulses to broaden their spectra is quite important for postcompression techniques [1]. On the other hand, broadening spectra as widely as possible is now a strong requirement for optimizing spectroscopic absorption-based LIDARs [light detection and ranging (systems)] in remote sensing techniques [38].

Figure 10 shows various spectral broadenings reached for different wavelengths. From the distances mentioned in this figure, the spectra were seen to keep almost the same shape at further propagation distances. Figures 10(a) and 10(b) display spectral broadenings promoted by 586-nm and 248-nm pulses, respectively, at input powers $P_{\rm in}/P_{\rm cr} \simeq 1.5$ without pulse steepening effects ($T = T^{-1} = 1$). For the same power, Fig. 10(c) depicts the spectral enlargement attained by UV pulses when space-time focusing and self-steepening are taken into account. Self-phase modulation starts with broadening symmetrically the spectrum. As the pulse first forms a leading peak increasing in intensity through the competition between Kerr focusing and MPI, a strong spectral red shift occurs near the focus point $z \to z_c$. At this stage, the leading peak depleted by MPI displaces to more and more negative times. Further, MPA partly damps this enhanced redshifting. Pulse steepening, in contrast, promotes an important blue shift and lowers the MPI-redshifted pedestal.

From an analytical point of view, we may describe qualitatively this spectral dynamics by employing the following approximations. First, we assume that the MPI response behaves just as a static density plateau, so that the ratio ρ/A^2 is either zero or close to unity with $\partial_z(\rho/A^2) \simeq 0$. Second, we retain self-steepening to the detriment of space-time focusing (i.e., we neglect diffraction in Kerr-dominated regimes). Third, we model a short portion of the pulse, initially located at $t = t_0$ with width τ_0, as $A^2 = A_0^2/\cosh(\tau)$, $\tau(t) = (t - t_0)/\tau_0$, and suppose that the amplitude does not change too much compared with this ansatz. Solutions to Eqs. (18) and (19) read under these assumptions as

$$A^2 \simeq A_0^2/\cosh[\tau - 3QA^2/A_0^2], \tag{21}$$

$$\varphi \simeq t_p \omega_0 \tau_0 \int_{-\infty}^{\tau} (1 - \rho/A^2) d\tau' - t_p \omega_0 \sinh^{-1}[\sinh(\tau) - Q]. \tag{22}$$

These expressions yield the spectral broadening $\Delta\omega/\omega_0 = -\varphi_t/\omega_0 = -\Delta\lambda/\lambda_0$:

$$\frac{\Delta\lambda}{\lambda_0} \simeq (1 - \rho/A^2) - [1 + \{Q^2 - 2Q\sinh(\tau)\}/\cosh^2(\tau)]^{1/2}. \tag{23}$$

The parameter Q defined in the preceding section is related to the self-steepening term and it enables the formation of a singular shock dynamics in the limit $Q \to 2/3$. As long as $Q \ll 1$ and in the absence of MPI, variations in wavelength $\Delta\lambda/\lambda_0 \approx -Q\sinh(\tau)/\cosh^2(\tau)$ starting with $t_0 = 0$ are symmetric and represent the early broadening through SPM. When MPI forms a defocusing plateau, $\Delta\lambda/\lambda_0$ then becomes larger in the region where $\rho = 0$ (nondefocused leading pulse), than when $\rho \to A^2$ (defocused trail), for which the broadening is weak. Consequently, as the beam reaches the first focus point z_c, the dominant part of the pulse is the front edge formed at times $t \to t^*$, where A^2 remains untouched by plasma defocusing ($\rho = 0$). Here, MPI creates a strong redshifting (see also Ref. [39]). The occurrence of a trail takes place in the regime of full plasma coupling $\rho/A^2 \to 1$, which enlarges the spectrum to the opposite side. Finally, self-steepening induced at increasing Q inhibits the MPI redshifting and instead displaces more the spectrum to the blue side. As a result, this creates an asymmetric spectral broadening with a prominent blue shift ($\Delta\lambda < 0$ for $\tau > 0$, see also Refs. [19,40]). Importantly, the spectral broadening is all the narrower as the laser wavelength is small ($\Delta\lambda \propto \lambda_0$). Laser pulses operating at visible wavelengths widely broaden, which is not the case of UV beams. This property was already observed numerically in the framework of the atmospheric propagation [34]. It is again found and now justified for the propagation of fs pulses in argon. Since the physics is the same for both gaseous media (air and Ar), white light generated at $\lambda_0 = 586$ nm may be accompanied, at least at sufficient powers, by conical emission ranging colors inside a concentric rainbow [6].

VII. CONCLUSION

In summary, we performed an exhaustive study on the nonlinear propagation of femtosecond pulses in gases and examined more particularly the roles of GVD, MPI, MPA, and deviations to the slowly varying envelope approximation (pulse steepening terms). This was done in view of optimiz-

ing the propagation properties leading to an efficient pulse shortening via, essentially, the defocusing action of the electron plasma created in the wake of the laser field. Several features previously published in the literature were confirmed, as shock generation by pulse steepening [19,10] and differences in spectral broadenings according to the laser wavelength [34]. Others, as the dominant role of GVD over MPI at low powers, have been discovered. These properties have been explained analytically and shown to occur generically in noble gases as argon in pressure-gas cells.

Throughout this investigation, the pressure appeared as a promising key parameter that should further allow experimentalists to tune the plasma response and partly control induced temporal distortions. Two ways of achieving a significant pulse reduction by plasma defocusing were revealed: Either the pulse profile undergoes strong distortions in time, which results in a compressed shape exhibiting both leading and trailing peaks, with an overall FWHM extension being much shorter than the input pulse duration (see, e.g., Fig. 4), or at weak powers, asymmetry in the temporal components of the pulse profile may favor a single dominant peak with duration reduced to almost the optical cycle (see, e.g., Figs. 2 and 7).

At powers close to critical ($P_{in}/P_{cr}<2$), pulses follow the scenario of the ''dynamical spatial replenishment'' (DSR), which takes place slowly enough to pick up subpulses compressed to few-cycle durations. At higher powers ($P_{in}/P_{cr}>2$), the DSR model still applies. The decay of the pulse profile into trailing and leading peaks arises several times along the longitudinal axis. However, this process does not prevent from shaping the pulse within an optical structure of duration <10 fs, once the peak power has been decreased to near-critical levels by MPA dissipation.

Furthermore, we investigated two different laser wavelengths and showed that the propagation dynamics was basically identical for both of them, up to noticeable differences in the spectra that are more broadened for large wavelengths.

In conclusion, we believe that the present analysis supplies a rather complete overview of the different propagation patterns. This survey, supported by analytical arguments, should help in figuring out a more comprehensive picture of the physics of ultrashort pulse propagation and related properties of duration shortening. We hope that this work will invite experimentalists in ultrafast optics to reach an accurate control of the nonlinearities which a femtosecond self-focusing pulse may undergo along its optical path in transparent media.

[1] M. Nisoli, S. de Silvestri, O. Svelto, R. Szipöcs, K. Ferencz, Ch. Spielmann, S. Sartania, and F. Krausz, Appl. Phys. B: Lasers Opt. **65**, 186 (1997).

[2] E. Mével, O. Tcherbakoff, F. Salin, and E. Constant, J. Opt. Soc. Am. B **20**, 105 (2003).

[3] M. Mlejnek, E.M. Wright, and J.M. Moloney, Opt. Lett. **86**, 1006 (1998).

[4] A. Braun, G. Korn, X. Liu, D. Du, J. Squier, and G. Mourou, Opt. Lett. **20**, 73 (1995).

[5] A. Brodeur, C.Y. Chien, F.A. Ilkov, S.L. Chin, O.G. Kosareva, and V.P. Kandidov, Opt. Lett. **22**, 304 (1997).

[6] O.G. Kosareva, V.P. Kandidov, A. Brodeur, C.Y. Chien, and S.L. Chin, Opt. Lett. **22**, 1332 (1997); E.T.J. Nibbering, P.F. Curley, G. Grillon, B.S. Prade, M.A. Franco, F. Salin, and A. Mysyrowicz, *ibid.* **21**, 62 (1996).

[7] E.T.J. Nibbering, G. Grillon, M.A. Franco, B.S. Prade, and A. Mysyrowicz, J. Opt. Soc. Am. B **14**, 650 (1997).

[8] S. Henz and J. Herrmann, Phys. Rev. A **59**, 2528 (1999).

[9] L. Bergé and A. Couairon, Phys. Rev. Lett. **86**, 1003 (2001).

[10] H. Ward and L. Bergé, Phys. Rev. Lett. **90**, 053901 (2003).

[11] J.H. Marburger, Prog. Quantum Electron. **4**, 35 (1975).

[12] H.R. Lange, G. Grillon, J.-F. Ripoche, M.A. Franco, B. Lamouroux, B.S. Prade, A. Mysyrowicz, E.T.J. Nibbering, and A. Chiron, Opt. Lett. **23**, 120 (1998).

[13] L. Bergé and A. Couairon, Phys. Plasmas **7**, 210 (2000).

[14] M. Nurhuda, A. Suda, M. Hatayama, K. Nagasaka, and K. Midorikawa, Phys. Rev. A **66**, 023811 (2002).

[15] P. Chernev and V. Petrov, Opt. Lett. **17**, 172 (1992).

[16] G.G. Luther, A.C. Newell, and J.V. Moloney, Physica D **74**, 59 (1994).

[17] G.G. Luther, J.V. Moloney, A.C. Newell, and E.M. Wright, Opt. Lett. **19**, 862 (1994).

[18] K. Germaschewski, R. Grauer, L. Bergé, V.K. Mezentsev, and J. Juul Rasmussen, Physica D **151**, 175 (2001); L. Bergé, K. Germaschewski, R. Grauer, and J. Juul Rasmussen, Phys. Rev. Lett. **89**, 153902 (2002).

[19] A.L. Gaeta, Phys. Rev. Lett. **84**, 3582 (2000).

[20] A. Couairon, S. Tzortzakis, L. Bergé, M. Franco, B. Prade, and A. Mysyrowicz, J. Opt. Soc. Am. B **19**, 1117 (2002).

[21] M. Mlejnek, E.M. Wright, and J.M. Moloney, Phys. Rev. E **58**, 4903 (1998).

[22] M.D. Feit and J.A. Fleck, Appl. Phys. Lett. **24**, 169 (1974).

[23] T. Brabec and F. Krausz, Phys. Rev. Lett. **78**, 3282 (1997).

[24] L.V. Keldysh, Zh. Éksp. Teor. Fiz. **47**, 1945 (1964) [Sov. Phys. JETP **20**, 1307 (1965)].

[25] M.D. Perry, O.L. Landen, A. Szöke, and E.M. Campbell, Phys. Rev. A **37**, 747 (1988).

[26] S. Skupin, U. Peschel, C. Etrich, L. Leine, F. Lederer, and D. Michaelis, Opt. Quantum Electron. **35**, 573 (2003).

[27] J. Schwarz, P. Rambo, and J.C. Diels, Appl. Phys. B: Lasers Opt. **72**, 343 (2001).

[28] J. Juul Rasmussen and K. Rypdal, Phys. Scr. **33**, 481 (1986).

[29] L. Bergé, Phys. Rep. **303**, 259 (1998).

[30] G. Fibich and G. Papanicolaou, SIAM (Soc. Ind. Appl. Math.) J. Appl. Math. **60**, 183 (1999).

[31] L. Bergé and A. Couairon, Physica D **152**, 752 (2002).

[32] S. Tzortzakis, B. Lamouroux, A. Chiron, M. Franco, B. Prade, and A. Mysyrowicz, Opt. Lett. **25**, 1270 (2000); S. Tzortakis, B. Lamouroux, A. Chiron, S.D. Moustaizis, D. Anglos, M. Franco, B. Prade, and A. Mysyrowicz, Opt. Commun. **197**, 131 (2001).

[33] J. Schwarz, P. Rambo, J.-C. Diels, M. Kolesik, E.M. Wright, and J.V. Moloney, Opt. Commun. **180**, 383 (2000).

[34] A. Couairon and L. Bergé, Phys. Rev. Lett. **88**, 135003 (2002).
[35] G. Fibich and G.C. Papanicolaou, Opt. Lett. **22**, 1379 (1997).
[36] J.K. Ranka and A.L. Gaeta, Opt. Lett. **23**, 534 (1998).
[37] D. Anderson and M. Lisak, Phys. Rev. A **27**, 1393 (1983).
[38] L. Wöste, C. Wedekind, H. Wille, P. Rairoux, B. Stein, S. Nikolov, C. Werner, S. Niedermeier, F. Ronneberger, H. Schillinger, and R. Sauerbrey, Laser Optoelektron. **29**, 51 (1997).
[39] Th. Lehner and N. Auby, Phys. Rev. E **61**, 1996 (2000).
[40] G. Yang and Y.R. Shen, Opt. Lett. **9**, 510 (1984).